

Molecular Rotations, Multiscale Order, Hyperuniformity, and Signatures of Metastability during the Compression/Decompression Cycles of Amorphous Ices

Published as part of *The Journal of Physical Chemistry virtual special issue "Pablo G. Debenedetti Festschrift"*.

Maud Formanek, Salvatore Torquato, Roberto Car, and Fausto Martelli*



Cite This: *J. Phys. Chem. B* 2023, 127, 3946–3957



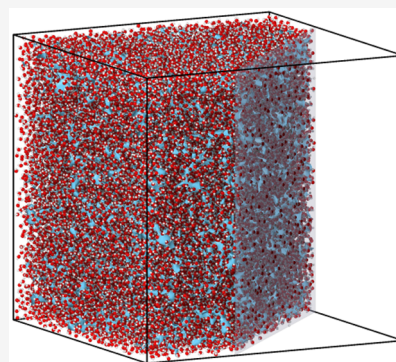
Read Online

ACCESS |

Metrics & More

Article Recommendations

ABSTRACT: We model, via large-scale molecular dynamics simulations, the isothermal compression of low-density amorphous ice (LDA) to generate high-density amorphous ice (HDA) and the corresponding decompression extending to negative pressures to recover the low-density amorphous phase (LDA_{HDA}). Both LDA and HDA are nearly hyperuniform and are characterized by a dynamical HBN, showing that amorphous ices are nonstatic materials and implying that nearly hyperuniformity can be accommodated in dynamical networks. In correspondence with both the LDA-to-HDA and the HDA-to- LDA_{HDA} phase transitions, the (partial) activation of rotational degrees of freedom activates a cascade effect that induces a drastic change in the connectivity and a pervasive reorganization of the HBN topology which, ultimately, break the samples' hyperuniform character. Key to this effect is the rapid rate at which changes occur, and not their magnitude. The inspection of structural properties from the short- to the long-range shows that signatures of metastability are present at all length-scales, hence providing further solid evidence in support of the liquid–liquid critical point scenario. LDA and LDA_{HDA} differ in terms of HBN and structural properties, implying that they are distinct low-density glasses. Our work unveils the role of molecular rotations in the phase transitions between amorphous ices and shows how the unfreezing of rotational degrees of freedom generates a cascade effect that propagates over multiple length-scales. Our findings greatly improve our basic understanding of water and amorphous ices and can potentially impact the field of molecular network-forming materials at large.



INTRODUCTION

The simple molecular structure of water hides a remarkably wide list of anomalous behaviors that stretch over the most complex phase diagram of any pure substance¹ and whose origin has been associated with a metastable critical point located at low temperatures and low pressures.^{2–6}

At deeply supercooled conditions, water exhibits polymorphism; i.e., it can exist in more than one glassy state. Indeed, the most common forms of glassy solid water are the low-density (LDA) and high-density amorphous (HDA) ices,^{7–16} which are structurally connected to their liquid counterparts at equilibrium conditions.¹⁷ The complex behavior of glassy solid water is reflected in the fact that LDA and HDA seem to encompass a larger set of subfamilies characterized by different structural properties, such as LDA-I and LDA-II,¹⁸ a more ordered low-density phase obtained upon heating ice VIII,¹⁹ expanded (e)HDA,²⁰ and a very high density (v)HDA.^{21,22} In this work, we classify our amorphous ices in terms of LDA and HDA unless otherwise specified.

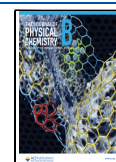
LDA and HDA are drastically different, with HDA being more than 20% denser than LDA, and can be interconverted

by, e.g., isothermal compression/decompression, via an apparent first-order-like phase transition,^{7,23–26} or by isobaric heating at different pressures.²⁷ At small length scales, LDA is reminiscent of hexagonal ice Ih, with water molecules forming four hydrogen bonds (HBs) with their (four) nearest neighbors and a hydrogen bond network (HBN) that is tetrahedrally coordinated. Indeed, LDA and Ih are characterized by comparable spectroscopic signals.¹ As for the case of Ih, and in contrast with the case of HDA, in LDA the first and the second shells of neighbors are well separated. The higher density of HDA is due to the presence of water molecules in the region between the first and the second shell of neighbors, thus acquiring distorted local configurations that strongly deviate from a perfect tetrahedral network. Despite such

Received: January 27, 2023

Revised: March 29, 2023

Published: April 11, 2023



marked differences in density, both amorphous ices are endowed with the surprising capability of partially suppressing long-range density fluctuations and are, therefore, nearly hyperuniform.^{28,29}

Broadly speaking, the network topology in disordered materials is an important descriptor for understanding the nature of the disorder that is usually hidden in pairwise correlations. Recently, it has been shown that the structural and dynamical properties of liquid water are related to the HBN topology in both bulk,^{30,31} as well as under confinement,^{32–35} and that water's anomalous behaviors are intimately linked to it.^{31,36} As shown in ref 31, the topology of the HBN and its dynamics can not be considered as separated entities, as they both define and affect large-scale properties.³¹ Similarly, the network of bonds dictates the degree of hyperuniformity in several other materials.^{37–40}

In this article, we show how the activation of molecular rotations triggers a cascade effect that propagates over multiple length scales, ultimately breaking the samples' hyperuniform character. We simulate the isobaric freezing of liquid water from ambient temperature to $T = 80$ K, and the isothermal LDA-to-HDA compression and the corresponding HDA-to-LDA_{HDA} decompression at four working temperatures, namely $T = 80$ K, $T = 100$ K, $T = 120$ K, and $T = 140$ K. For each thermodynamic condition, we inspect the short-range order, the large-scale properties, and the topology of the HBN as well as its dynamics.

The article is organized as follows. The computational details are presented in **Computational Details**. In **Results**, we describe the results of our investigations. Finally, in **Conclusions**, we present our conclusions.

■ COMPUTATIONAL DETAILS

Numerical Setup. Our study is based on classical molecular dynamics (MD) simulations of a system composed of $N = 50000$ rigid water molecules described by the TIP4P/2005 interaction potential⁴¹ in the isobaric (NPT) ensemble. This water model is able to reproduce relatively well the structures of LDA and HDA at low temperatures.⁴² We perform extensive out-of-equilibrium simulations using the GROMACS 2018.1 software package⁴³ with GPU acceleration. Coulombic and Lennard-Jones interactions are calculated with a cutoff distance of 1.1 nm and long-range electrostatic interactions are treated using the Particle-Mesh Ewald (PME) algorithm. Temperatures and pressures are controlled using a Nosé–Hoover thermostat^{44,45} and a Berendsen barostat.⁴⁶ For the Nosé–Hoover thermostat, the period of the kinetic energy oscillations between the system and the reservoir is set to 1 ps; the time constant for the Berendsen barostat is set to 1 ps.

We prepare LDA by cooling the equilibrium liquid from $T = 300$ K to $T = 80$ K using a cooling rate of $q_c = 1$ K/ns. In order to prepare HDA, we compress the so-formed LDA from ambient pressure to $P = 2.0$ GPa at four different temperatures, namely $T = 140$ K, $T = 120$ K, $T = 100$ K, and $T = 80$ K with a compression rate of $q_p = 0.01$ GPa/ns. We then model the corresponding isothermal decompression of HDA to -0.5 GPa with a decompression rate equal to q_p . The results reported in this work are the average of 5 independent simulations.

Tetrahedral Order Parameter. We quantify the local tetrahedrality by using the local order metric (LOM) and the score function F defined in ref 47. Briefly, the score function measures the degree of overlap between the neighborhood (called pattern) of a given water molecule j and the reference

structure of a perfect solid. In this work we have analyzed the degree of tetrahedrality; i.e., we have adopted as a reference structure a perfect tetrahedron, and we have analyzed how close to such structure the first shell of neighbors of each water molecule in the system is.

For a given orientation of the reference structure and a given permutation \mathcal{P} of the pattern indices, we define a local order metric $F(j)$ as the maximum overlap between pattern and reference structure in the j neighborhood by

$$F(j) = \max_{\theta, \phi, \psi; \mathcal{P}} \left\{ \prod_{i=1}^M \exp \left(- \frac{|\mathbf{P}_{i\mathcal{P}}^j - \mathbf{A}^j \mathbf{R}_i^j|^2}{2\sigma^2 M} \right) \right\} \quad (1)$$

where θ , ϕ , and ψ are Euler angles, $\mathbf{P}_{i\mathcal{P}}^j$ and \mathbf{R}_i^j are the pattern and the reference position vectors in the laboratory frame of the M neighbors of site j , respectively, and \mathbf{A}^j is an arbitrary rotation matrix about the pattern centroid. The parameter σ controls the spread of the Gaussian functions ($\sigma = d/4$ in this work, where d is the characteristic length of the local pattern). The LOM satisfies the inequalities $0 \leq F(j) \leq 1$. The two limits correspond, respectively, to a local pattern with randomly distributed points ($F(j) \rightarrow 0$) and to an ordered local pattern matching perfectly the reference ($F(j) \rightarrow 1$). We also define a global order parameters based on $F(j)$, as the average score function F :

$$F = \frac{1}{N} \sum_{j=1}^N F(j) \quad (2)$$

The details of the numerical algorithm can be found in ref 47. The local order metric and the score function are sensitive and versatile metrics.^{25,31,35,36,47,48,48–52} In the case of amorphous ices, they have helped in uncovering a link between HDA and the metastable high-pressure ice IV.²⁵

Network Topology. We investigate the topology of the HBN as a function of the temperature and pressure using the ring statistics, a theoretical tool that has been instrumental in understanding the properties of water at different thermodynamic conditions,^{2,25,30,31,36,50,53–56} water under confinement,^{32,33,35} aqueous solutions,^{57–60} amorphous systems,^{61,62} clathrate hydrates,⁶³ and phase-change materials^{51,64} and is essential to characterize continuous random networks.^{65–72}

In order to compute the ring statistics, it is necessary to define the link between atoms/molecules. Possible definitions can be based on the formation of bonds, interaction energies, geometric distances, etc. The second step is the definition of ring and the corresponding counting scheme. This task is of particular relevance in directional networks, like water or silica, where the donor/acceptor nature of the bonds breaks the symmetry in the linker search path. Several definitions of rings and counting schemes have been reported in the literature.^{61,62,73–77}

Depending on how links are constructed and ring counted, different topologies are explored carrying complementary information.⁵⁴ In this work, we adopt the following counting scheme which has been shown to carry the most information about the HBN⁵⁴ and to directly connect its topology with properties of water such as translational diffusion, rotational dynamics, and short- and intermediate-range order:³⁰ starting from a water molecule, we construct rings recursively traversing the HBN until the starting point is reached again or the path exceeds the maximal ring size considered (12 water molecules in our case). We consider primitive rings only, i.e.,

rings that can not be reduced to smaller ones. In this study, we do not discern among the acceptor/donor character of the starting water molecule.⁵⁴

The definition of hydrogen bond (HB) follows ref 78. In this regard, any quantitative measure of HBs in liquid water is somewhat ambiguous, since the notion of an HB itself is not uniquely defined. However, a qualitative agreement between many proposed definitions has been deemed satisfactory over a wide range of thermodynamic conditions.^{79,80}

Hyperuniformity, Long-Range Density Fluctuations, and Multiscale Metric τ . Central to the concept of hyperuniformity⁸¹ is the structure factor $S(k)$. In the thermodynamic limit,

$$S(k) = 1 + \rho \tilde{h}(k) \quad (3)$$

where $\tilde{h}(k)$ is the Fourier transform of the total correlation function (pair correlation function minus one) and k is the wavevector. The vanishing of normalized long-range density fluctuations in hyperuniform systems implies that $S(k) \rightarrow 0$ for $k \rightarrow 0$, where $k = |k|$ is the wavenumber and $S(k)$ is the structure factor $S(k)$ averaged over all directions at wavevector k . A useful practical measure of the degree of hyperuniformity in a system is provided by the hyperuniformity index

$$H \equiv \frac{S(0)}{S(k_{\text{peak}})} \quad (4)$$

where k_{peak} is the wavenumber k at which $S(k)$ has its maximal peak value. Systems in which $H \sim 10^{-3}$ or smaller are deemed to be nearly or effectively hyperuniform.⁸² The reference state that is used in the definition of H , i.e., the normalization of $S(0)$ with respect to $S(k_{\text{peak}})$, derives from how the scattering intensity evolves as density increases from a low-density phase to a perfectly hyperuniform state. At very low densities, the scattering pattern is very uniform because the particles are spatially uncorrelated, but as the density increases, there is increasingly less scattering around the origin, and increasingly a dominant higher-intensity concentric ring emerges around the origin located in the vicinity of wavenumber k_{peak} . Thus, the value $S(k_{\text{peak}})$ is an important reference state to be compared to $S(0)$.

The volume integral of the square of the radial distribution function (and, therefore, of the structure factor in the Fourier space, using the Parseval theorem) provides a useful metric τ that captures the degree of translation order/disorder across all length scales, including positive and negative correlations.⁸³ The order metric τ is defined as

$$\tau \equiv \frac{1}{\rho^d} \int_{\mathbb{R}^d} [g_{OO}(r) - 1]^2 dr \quad (5)$$

where ρ is the number density and d the dimension of the Euclidean space ($d = 3$ in this work). In the thermodynamic limit, τ diverges for perfect crystals while it vanishes identically for spatially uncorrelated systems. Thus, a deviation of τ from zero, which can only be positive, measures the degree of translational order relative to the fully uncorrelated case.

RESULTS

In this section, we report the main results of our study describing the isothermal interconversion between amorphous ices.

Density Profiles. We start our investigation by inspecting the density profile during the compression/decompression

cycles. Our results, reported in Figure 1, show a clear hysteresis with a pronounced jump during the compression (black) and a

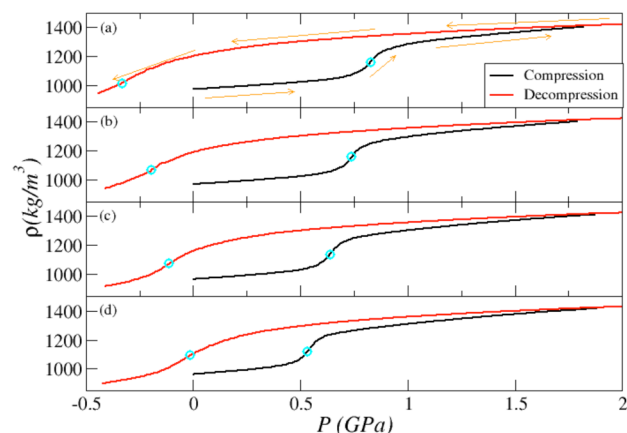


Figure 1. Density profiles for the compression (black solid line) and decomposition (red solid line) cycles at the four temperatures explored in this work. Panel a reports the cycle at $T = 80$ K, panel b at $T = 100$ K, panel c at $T = 120$ K, and panel d at $T = 140$ K. The arrows represent the direction of the compression/decompression. The circles represent the loci of the inflection points.

smoother profile during the decomposition (red). In panel a, we report the cycle at $T = 80$ K, in panel b, at $T = 100$ K, in panel c, at $T = 120$ K, and in panel d, the cycle at $T = 140$ K. The presence of hysteresis in the compression/decompression cycles supports the hypothesis that LDA and HDA are separated by a first-order phase transition. In Figure 1, we emphasize with cyan circles, the inflection points during the phase transitions. It is possible to observe that the cycles shrink upon increasing the working temperature, as is clearly visually appreciable looking at the loci of the inflection points. The reduction between the inflection points observed upon increasing the temperature suggests a convergence at thermodynamic conditions which might correspond to the liquid–liquid critical point. In order to test this hypothesis, in Figure 2, we report the inflection points, as a function of the temperature. The dashed lines are obtained upon fitting the four points during the compression (black line) and the decomposition (red line). The fitted values merge at the thermodynamic point $T \sim 180$ K and $P \sim 0.27$ GPa, not far

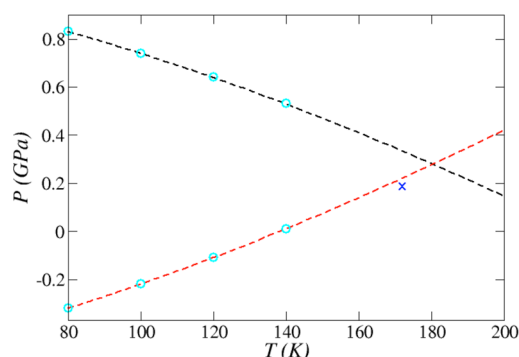


Figure 2. Inflection points of the densities (cyan symbols) computed during our simulations. The dashed lines represent the profile of the inflection points obtained by fitting the available data. The blue symbol represents the liquid–liquid critical point located at $T_c = 172 \pm 1$ K and $P_c = 0.1861 \pm 0.009$ GPa for this model of water.⁴

from the reported thermodynamic point at which this model of water shows a liquid–liquid critical point. i.e., $T_c = 172 \pm 1$ K and $P_c = 0.1861 \pm 0.009$ GPa⁴ (blue symbol in the figure).

Short-Range Order. In Figure 3, we report the evolution of the degree of short-range order quantified via the score

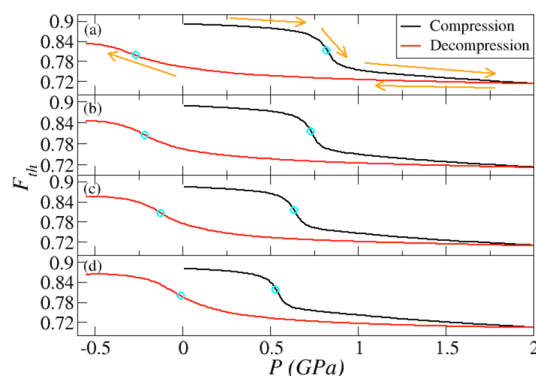


Figure 3. Global tetrahedral order parameter F_{th} for the compression (black solid line) and decompression (red solid line) cycles at the four temperatures explored in this work. Panel a reports the cycle at $T = 80$ K, panel b at $T = 100$ K, panel c at $T = 120$ K, and panel d at $T = 140$ K. The arrows represent the direction of the compression/decompression. The circles represent the loci of the inflection points.

function F_{th} (eq 2) obtained using, as a reference structure, a perfect tetrahedron. At all temperatures, LDA is characterized by a value of tetrahedrality as high as $F_{th} \sim 0.9$, expressing the highly tetrahedral order of the first shell of neighbors which is comparable to, but not equal to, hexagonal ice. The value of F_{th} drops in correspondence with the phase transition to HDA; the (well-known) reduction of the tetrahedral character in HDA is caused by the approaching of water molecules from the second shell of neighbors to the first shell of neighbors. Thermal energy facilitates molecular rearrangements, and as a result, the transition to HDA occurs at progressively lower pressures upon increasing the temperature of the sample, in agreement with ref 27. Upon further increasing the pressure exerted on the sample of HDA, we observe a continuous reduction in the value of F_{th} indicating that the first shell of neighbors becomes progressively more and more distorted due to the increasing number of water molecules populating the space between the first and the second shell of neighbors. Upon decompressing the sample of HDA, we observe that LDA is recovered only at low or negative pressures, as reported by the value of F_{th} , which increases back to values characteristic of a highly tetrahedral first shell of neighbors. In the case of $T = 80$ K, F_{th} shows a significant increase only at negative pressures while at higher temperatures, the increase occurs closer to ambient pressure. Interestingly, the samples of LDA_{HDA} are characterized by lower values of F_{th} compared to the samples of LDA at the same temperature. Therefore, the two low-density amorphous ices are structurally different but belong to the same family of LDA.

The presence of hysteresis in the compression/decompression cycles supports the hypothesis that LDA and HDA are separated by a first-order phase transition. It is possible to appreciate how the distance, in terms of pressure, between the inflection points in F_{th} during the compression/decompression cycles (blue circles in the figure) tends to decrease upon increasing the temperature, suggesting a convergence at thermodynamic conditions which might correspond to the

liquid–liquid critical point. In order to test this hypothesis, in Figure 4 we report the inflection points of F_{th} (cyan circles)

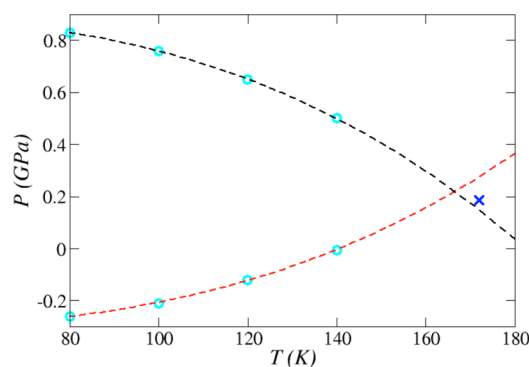


Figure 4. Inflection points of F_{th} (cyan symbols) obtained during our simulations. The dashed lines represent the profile of the inflection points obtained by fitting the available data. The blue symbol represents the liquid–liquid critical point located at $T_c = 172 \pm 1$ K and $P_c = 0.1861 \pm 0.009$ GPa for this model of water.⁴

shown in Figure 3, as a function of the temperature. The dashed lines are obtained upon fitting the four points during the compression (black line) and the decompression (red line). The fitted values merge at the thermodynamic point $T = 167$ K and $P = 0.22$ GPa, not far from the reported thermodynamic point at which this model of water shows a liquid–liquid critical point, i.e., $T_c = 172 \pm 1$ K and $P_c = 0.1861 \pm 0.009$ GPa⁴ (blue symbol in the figure). Therefore, manifestations of metastable criticality are embedded at the level of short-range order.

Isothermal Compression of LDA. Panel a in Figure 5 reports the two-body pair correlation function $g_{OO}(r)$

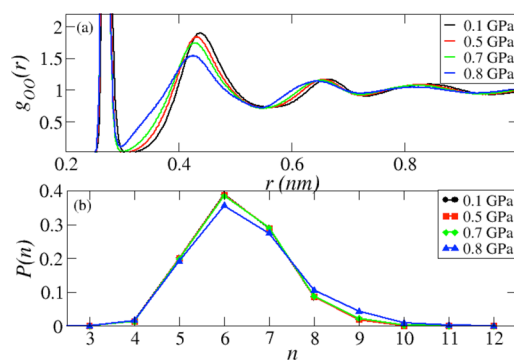


Figure 5. Panel a: two-body pair correlation functions computed among water's oxygen atoms only for LDA at different pressures and $T = 80$ K. The black solid line reports the $g_{OO}(r)$ for $P = 0.1$ GPa, the red line for $P = 0.5$ GPa, the green line for $P = 0.7$ GPa, and the blue line for $P = 0.8$ GPa, roughly corresponding to the onset of the phase transition at this temperature. Panel b: normalized probability distribution $P(n)$ of having a ring of length n in the samples reported on panel a.

computed among oxygen atoms only, for LDA at different pressures and at $T = 80$ K. Similar results hold for all the other temperatures here simulated and are therefore not shown. At low pressures, LDA is characterized by well-separated first and second hydration shells, with well-defined shells of neighbors at larger distances. The overall structure of LDA is fairly insensitive to the applied pressure: upon increasing the

pressure from $P = 0.1$ GPa to $P = 0.5$ GPa and $P = 0.7$ GPa the first and the second peak remain well separated with only a slight decrease in the intensity of the second and higher peaks that slightly shifts closer to the first peak. Upon further increasing the pressure to $P = 0.8$ GPa (blue line), roughly corresponding to the onset of the phase transition at $T = 80$ K,^{25,28} the space between the first and the second peak starts to be populated and the second peak reports a relevant decrease in intensity. Nonetheless, higher peaks are still well-defined.

Panel b in Figure 5 shows the topologies of the HBN for the thermodynamic states reported in the panel a. In particular, we here report $P(n)$, the normalized probability of having a ring of length n . At low pressures, LDA is characterized by a distribution $P(n)$ peaked at $n = 6$ which represents hexagonal rings. At these thermodynamic conditions, $n = 6$ represents $\sim 40\%$ of the overall topology. Other relevant geometries present in the network are pentagons ($n = 5$, accounting for $\sim 20\%$ of the total configurations), heptagons ($n = 7$, accounting for $\sim 30\%$), and octagons ($n = 8$, accounting for $\sim 10\%$). Shorter and longer rings mostly do not contribute. As for the two-body pair correlation function, $P(n)$ is mostly unaffected by the increasing pressure. In correspondence with the onset of the phase transition, at $P = 0.8$ GPa, we observe a small change in the $P(n)$ characterized by a decrease in hexagons and heptagons and an increase in longer rings (in particular $n = 9$ which accounts for $\sim 5\%$ of the overall topology) and which accounts for the increase in the sample density. Interestingly, we can observe that the contribution of $n = 12$ is almost null even at the highest pressures, indicating water molecules do not arrange in rings longer than $n = 12$. As a matter of fact, for this model of water configurations with $n > 12$ disappear in liquid water at ambient pressure and $T < 240$ K.³¹

Upon further increasing the pressure, the sample undergoes a phase transition characterized by an abrupt change in the structural properties and in the network topology. In panel a of Figure 6, we report the $g_{OO}(r)$ computed among water's oxygen atoms in the pressure window $P \in [0.8\text{--}1.1]$ GPa, corresponding to the window in which LDA transitions to HDA at $T = 80$ K. We can observe that increasing the pressure from $P = 0.80$ GPa (black line) to $P = 0.85$ GPa (red line) a left shoulder on the second peak starts appearing. This

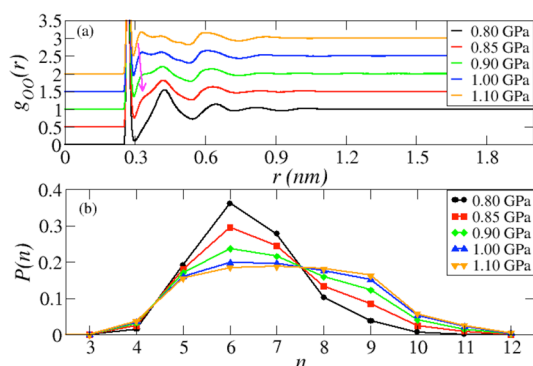


Figure 6. Panel a: two-bodies pair correlation functions computed among water's oxygen atoms only in correspondence with the phase transition at $T = 80$ K. The black solid line reports the $g_{OO}(r)$ for $P = 0.8$ GPa, the red line for $P = 0.9$ GPa, the green line for $P = 1.0$ GPa and the blue line for $P = 1.1$ GPa. Panel b: normalized probability distribution $P(n)$ of having a ring of length n in the samples reported on panel a.

shoulder indicates that water molecules on the second hydration shell start to approach the first hydration shell, further increasing the density of the sample. The shoulder becomes more pronounced upon increasing the pressure to $P = 0.90$ GPa (green line), at which the fourth and fifth peaks are no longer defined. At $P = 1.0$ GPa (blue line), the shoulder and the main second peak become equally intense, and the shoulder becomes more intense at $P = 1.1$ GPa (orange line). Interestingly, at this pressure, we can observe the formation of another shoulder in between the second and third hydration shells, emphasized by the arrow in the figure.

The structural changes occurring in correspondence with the LDA-to-HDA phase transition reported in panel (b) of Figure 6 can occur because water molecules can change their connectivity via a pervasive rearrangement of the HBN, as shown in panel (b) of Figure 6 where we report the distribution $P(n)$. We can observe that moving from $P = 0.8$ GPa to $P = 0.85$ GPa the network topology drastically changes. Hexagonal and heptagonal rings decrease in favor of longer rings. This tendency continues upon increasing the pressure, with the flattening of $P(n)$ and, eventually, at $P = 1.1$ GPa (orange line) the sample mostly hosts an equal amount of $n = 6$, $n = 7$, and $n = 8$ ($\sim 20\%$) as well as $n = 5$ and $n = 9$ ($\sim 15\%$) and longer rings such as $n = 10$ and $n = 11$.

In Figure 7, panel a, we report the structural properties as a function of the pressure for HDA up to $P = 2.0$ GPa. We can

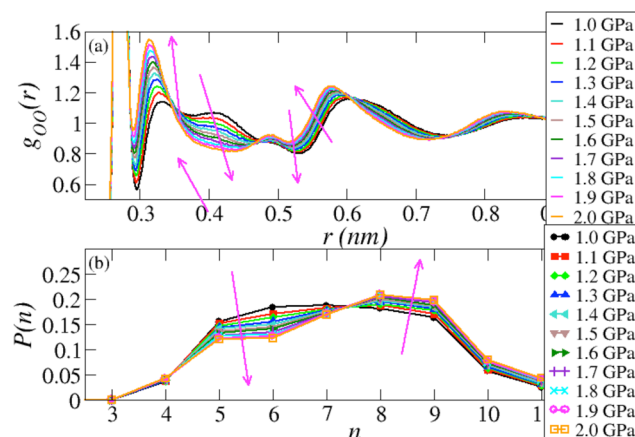


Figure 7. Panel a: two-bodies pair correlation functions computed among water's oxygen atoms as a function of the pressure. Panel b: normalized probability distribution $P(n)$ of having a ring of length n in the samples reported on panel a. Arrows indicate the direction of increasing pressure.

observe that, upon increasing the pressure, the intensity of the interstitial peak increases while the intensity of the shoulder decreases. In particular, we observe that the bimodality disappears at $P = 1.3$ GPa (blue line) in the region $r \in (0.3, 0.45)$. Interestingly, the region between $r = 0.45$ nm and $r = 0.55$ nm becomes increasingly more defined. The network topology corresponding to the phases just described is reported in panel b of Figure 7. At variance with LDA, for which the HBN topology is mostly independent of the pressure exerted on the sample, the HBN topology of HDA keeps changing with the pressure. Upon increasing the pressure we observe a systematic decrease in rings shorter than $n = 8$ and a corresponding increase in the longer rings. At the highest pressure here simulated, $P = 2.0$ GPa, the sample mostly hosts $n = 8$ and $n = 9$ configurations, which together

account for $\sim 40\%$ of the overall topology. The configuration $n = 7$ accounts for $\sim 17\%$, while $n = 6$ and $n = 5$ decrease to less than 15% each. It is worth mentioning, at this point, that rings $n > 12$ are still not present in any of the HDA samples simulated in this work. Considering that the second shell of neighbors collapses toward the first shell of neighbors, one may ask the question of whether a given water molecule is bonded to the interstitial molecules in HDA. As a matter of fact, we find that in HDA a given water molecule never binds to the interstitial neighbors. This can be seen in Figure 8, reporting a

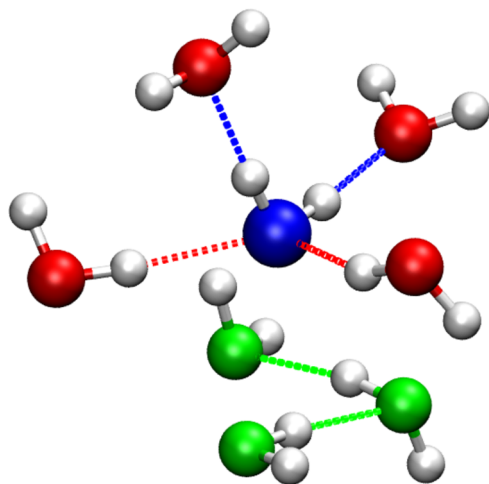


Figure 8. Representative snapshot of water molecules extracted in HDA at $P = 2$ GPa. The oxygen of the central water molecule is emphasized in blue; the oxygens of the four nearest neighbors are reported in red, while the interstitial water molecules are emphasized in green. The red dashed lines represent the HBs accepted by the central molecule, while the blue dashed lines represent the HBs donated by the central molecule. It is possible to observe how the interstitial molecules are not bonded to the central molecule.

representative snapshot of water molecules in HDA at $P = 2.0$ GPa. The blue molecule is the central water molecule that is donating two HBs (blue dashed lines) and is accepting two HBs (red dashed lines). These bonds occur in correspondence with the nearest neighbors. The interstitial molecules (green spheres) belong to a different network of bonds (green dashed lines). This observation is in agreement with recent observations on the network of bonds in supercooled liquid water at high pressures.⁸⁴

The rearrangement in the HBN occurring in correspondence with the phase transition from LDA to HDA is favored by partial activation of the rotational degrees of freedom which, in LDA, are otherwise frozen. In Figure 9, we report the rotational autocorrelation function $C_{rot}(t)$ for the isothermal compression of LDA at $T = 80$ K (upper panel) and at $T = 140$ K (lower panel) in the pressure ranges close to the LDA-to-HDA phase transitions. It is possible to observe how, in both cases, the rotational degrees of freedom partially unfreeze in correspondence with the phase transition (continuous line). Our findings support the experimental observation that molecular rotations drive the phase transition between LDA and HDA,⁸⁵ and go beyond showing how molecular rotations allow for a pervasive rearrangement of the HBN.

Isothermal Decompression of HDA. In Figure 10, panel a, we report the structural evolution of the HDA undergoing isothermal decompression at $T = 80$ K down to negative

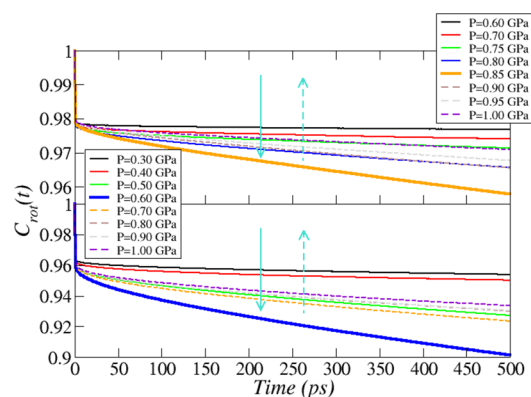


Figure 9. Rotational autocorrelation function $C_{rot}(t)$ for the isothermal compression of LDA at $T = 80$ K (upper panel) and at $T = 140$ K (lower panel). Continuous lines refer to the gradual unfreezing of molecular rotations, while dashed lines to the gradual freezing. Arrows indicate the direction of increasing pressure.

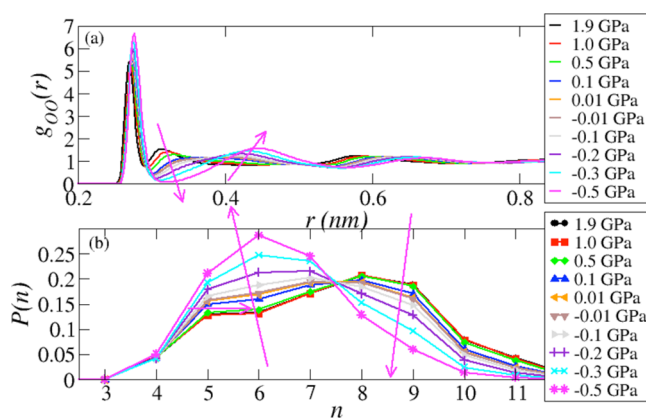


Figure 10. Panel a: two-body pair correlation functions computed among water's oxygen atoms as a function of the pressure during the isothermal decompression and at $T = 80$ K. Panel b: normalized probability distribution $P(n)$ of having a ring of length n in the samples reported on panel a. Arrows indicate the direction of decreasing pressure.

pressures in terms of $g_{OO}(r)$. We can observe that, upon decompressing HDA from high pressures to $P = 0.01$ GPa, the interstitial peak initially located at ~ 0.31 nm decreases in intensity, shifts to larger distances, and spreads to values in the range 0.34 – 0.43 nm, indicating that the water molecules populating the space between the first and the second shell of neighbors now tend to move farther away from the first shell and start rebuilding a second shell of neighbors characteristic of more ordered phases. Upon further decreasing the pressure, and reaching the negative pressure regime, we observe a gradual recovery of the $g_{OO}(r)$ characteristic of LDA with a shift of the third shell of neighbors toward larger distances. Therefore, at $T = 80$ K LDA is recovered only at negative pressures, namely between $P = -0.3$ GPa and $P = -0.5$ GPa.

From Figure 10, panel b, we can observe that the decompression from $P = 1.9$ GPa to $P = 1.0$ GPa does not modify substantially the topology of the HBN which maintains all the feature of HDA, i.e., a network dominated by long rings to account for the high density of the sample. Decreasing the pressure to $P = 0.1$ GPa to $P = 0.01$ GPa, the topology of the HBN undergoes a rearrangement but is still dominated by heptagonal rings and longer rings are present in

considerable amounts. Upon further decompressing the sample, the HBN recovers LDA-like distributions only at $P = -0.3$ GPa and $P = -0.5$ GPa, in agreement with the behavior of the $g_{OO}(r)$. It is worth emphasizing that the network topology of LDA_{HDA} never fully recovers that of LDA at ambient pressure (Figure 5, panel b), as its $P(n)$, contains $\sim 5\%$ less hexagonal rings, but similar networks are obtained when the decompression reaches the negative pressure $P \sim -0.3$ GPa. Therefore, LDA_{HDA} and LDA are two distinct glasses with distinct HBNs and structural properties (Figure 3). In particular, LDA_{HDA} is more disordered than LDA, hence implying that the decompression of HDA does not lead to any crystallization.⁸⁶

In Figure 11, panel a, we report the evolution of the $g_{OO}(r)$ as a function of the pressure for $T = 140$ K. Qualitatively

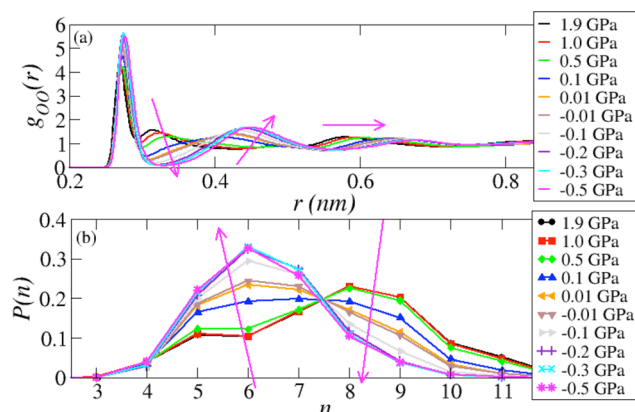


Figure 11. Panel a: two-bodies pair correlation functions computed among water's oxygen atoms as a function of the pressure during the isothermal decompression and at $T = 140$ K. Panel b: normalized probability distribution $P(n)$ of having a ring of length n in the samples reported on panel a. Arrows indicate the direction of decreasing pressure.

speaking, the $g_{OO}(r)$ s acquire a similar profile as at $T = 80$ K (Figure 5). We can observe a gradual decrease of the interstitial peak and a corresponding development of the second peak, a shift toward larger distances of the third peak, and an increase in the intensity of the first peak. The $g_{OO}(r)$ of LDA is recovered at $P = -0.1$ GPa, i.e., at higher pressures with respect to the case of $T = 80$ K. Intermediate temperatures, namely $T = 100$ K and $T = 120$ K, fall in between, indicating that the recovery of LDA is effectively a thermally induced process.

Panel b of Figure 11 reports the evolution of $P(n)$ as a function of the pressure for the decompression of HDA at $T = 140$ K. We can observe that, at high pressures, the HBN hosts longer rings to accommodate the high density of the sample. In particular, from $P = 1.9$ GPa to $P = 0.5$ GPa the network is mostly dominated by rings of lengths $n = 8$, $n = 9$, and $n = 7$ and fairly independent of the pressure, reflecting the independence of the short-range order F_{th} in this pressure window (Figure 3d). Upon further decompressing the sample to $P = 0.1$ GPa, we recover the $P(n)$ typical of HDA obtained just after the phase transition from LDA to HDA (triangular symbols). This distribution is characterized by an almost equal contribution of $n = 6$, $n = 7$, and $n = 8$, a lower, roughly equal contribution of $n = 5$ and $n = 9$, and a lower contribution of lower rings. Moving to lower pressures, we observe a quite drastic change in the topology of the HBN from $P = 0.1$ GPa

to $P = 0.01$ GPa. The contribution of $n = 8$ and $n = 9$ reduces mostly in favor of $n = 6$ and $n = 7$ indicating that the hexagonal network characteristic of low-density phases is being recovered. On the other hand, as for $T = 80$ K, the network still hosts a considerable percentage of longer rings, and therefore, LDA and LDA_{HDA} are distinct glasses.

In order to understand if the rearrangements of the HBN are triggered by molecular rotations as in the phase transition from LDA to HDA, in Figure 12 we report the rotational

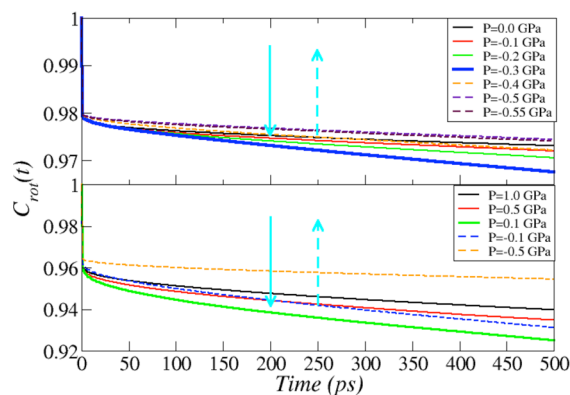


Figure 12. Rotational autocorrelation function $C_{rot}(t)$ for the isothermal decompression of HDA at $T = 80$ K (upper panel) and at $T = 140$ K (lower panel). Continuous lines refer to the gradual unfreezing of molecular rotations, while dashed lines refer to the gradual freezing. Arrows indicate the direction of increasing pressure.

autocorrelation function $C_{rot}(t)$ for the decompression of HDA. The upper panel reports $C_{rot}(t)$ for the decompression of HDA at $T = 80$ K and $P \in [0.0, -0.5]$ GPa, corresponding to the pressure window in which we observe the transformation to LDA_{HDA} . Upon decreasing the pressure from $P = 0.0$ GPa to $P = -0.3$ GPa (continuous lines), we observe a gradual unfreezing of molecular rotations, followed by a refreezing at lower pressures (dashed lines). Similarly, a partial unfreezing of molecular rotations occurs at $T = 140$ K (lower panel): the unfreezing takes place upon decompressing the sample from $P = 1.0$ GPa to $P = 0.1$ GPa. Therefore, we can state that the transformations between LDA, HDA, and LDA_{HDA} occur thanks to a partial unfreezing of molecular rotations which, ultimately, allow the HBN to explore a wider topological space acquiring different configurations. As we will see in the following discussion, the unfreezing of molecular rotations and the changes in the HBN topology affects the large-scale properties of amorphous ices.

Hyperuniformity during the Compression/Decompression Cycles. In this section, we extend previous investigations²⁸ exploring large-scale structures up to $T = 140$ K and during the compression/decompression cycles. The investigation of long-range density fluctuations encompasses important clues about the basic nature of water,^{28,29} as well as other disordered materials,⁸⁷ biological systems^{88,89} and prime numbers.⁹⁰ Both LDA and HDA samples at $T = 80$ K are endowed with the property of suppressing (up to some extent) long-range density fluctuations and are, therefore, nearly hyperuniform.²⁸

In Figure 13, we report the profile of the hyperuniformity index H (eq 4) during the compression/decompression cycles simulated in this work. The upper panel refers to $T = 80$ K, the middle panels to $T = 100$ K and $T = 120$ K, respectively, and

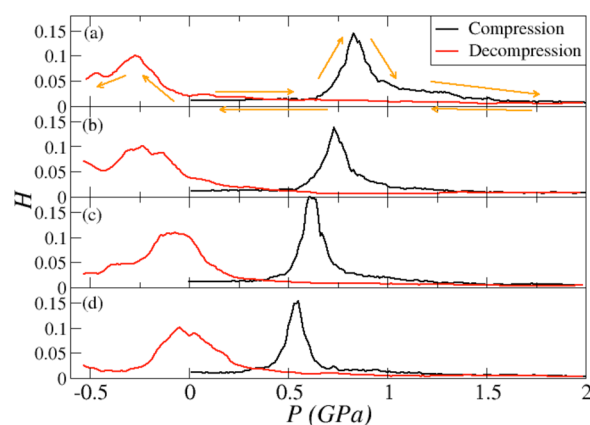


Figure 13. Profile of the H index for the compression (black line) and decompression (red line) of amorphous ices at $T = 80$ K (panel a), at $T = 100$ K (panel b), at $T = 120$ K (panel c) and at $T = 140$ K (panel d). The directions of the arrow report the direction of the compression/decompression cycles for the four temperatures.

the lower panel to $T = 140$ K. As previously reported, we can observe that both amorphous ices are endowed with the property of suppressing long-range density fluctuations more than the liquid phase. At all pressures, in correspondence with the LDA-to-HDA phase transitions, we observe a significant increase in the value of H indicating a loss of hyperuniformity and the appearance of long-range density fluctuations. Such fluctuations are induced by the partial activation of rotational degrees of freedom and the consequent rearrangement of the HBN previously described, and wear off upon further increasing the pressure, entering the domain of HDA. Upon decompressing the samples, we observe that H does not change appreciably until the pressure window of recovery of LDA, which is characterized by a further increase in the value of H . Therefore, the appearance of long-range density fluctuations in correspondence with the phase transitions is related to the rearrangement of the HBN which, as shown in panel a of Figures 6 and 10 undergoes a pervasive rearrangement in correspondence with both the LDA-to-HDA and the HDA-to-LDA phase transitions. In Figure 14, we report the loci of the maxima of H (cyan circles) shown in Figure 13. The black and red dashed lines represent the curve obtained upon fitting the values of the maxima of H at each

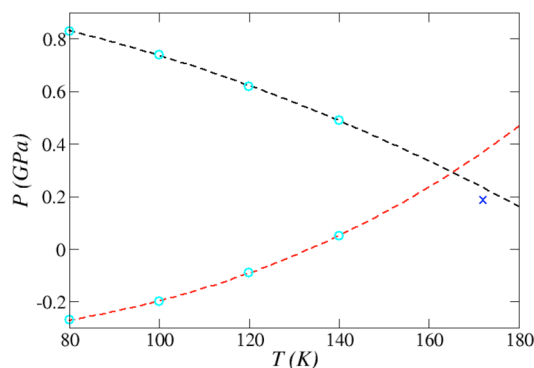


Figure 14. Loci of the maxima of H (cyan symbols) obtained during our simulations. The dashed lines represent the profile of the inflection points obtained by fitting the available data. The blue symbol represents the liquid–liquid critical point located at $T_c = 172 \pm 1$ K and $P_c = 0.1861 \pm 0.009$ GPa for this model of water.⁴

thermodynamic point. We can observe that the maxima tend to converge to a point ($T \sim 165$ K and $P \sim 0.29$ GPa) not far from the liquid–liquid critical point reported in ref 4.

Molecular rotations induce changes in the connectivity, i.e., in the neighbors of each water molecule. In Figure 15, we

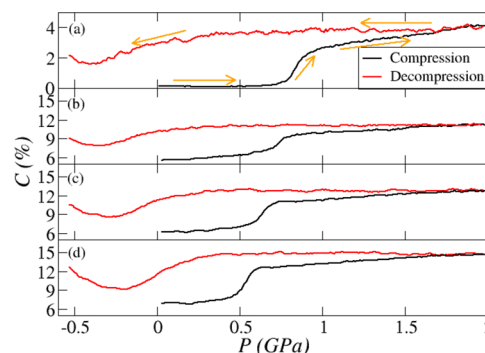


Figure 15. Percentage C of water molecules involved in one or more bond changes as a function of the applied pressure for $T = 80$ K in panel a, $T = 100$ K in panel b, $T = 120$ K in panel c, and $T = 140$ K in panel d. The black lines report C during the compression while the red lines report C during the decompression. The direction of the arrows in panel a indicates the compression/decompression cycles for all temperatures.

report C , the variation of connectivity between consecutive snapshots and averaged over 1 ns as a function of the applied pressure for the four temperatures here investigated. Panel a reports C as a function of the pressure for $T = 80$ K, panel b for $T = 100$ K, panel c for $T = 120$ K, and panel d for $T = 140$ K. The four compression/decompression cycles follow the directions of the arrow shown only in panel a.

From Figure 15a, we can observe that the percentage of water molecules changing neighbor(s) in LDA is on the order of 0.1%, implying that the HBN topology is stable and changes are minor and localized. In correspondence with the transformation pressure, we observe a jump in the value of C to values as high as $\sim 2\%$. This observation is a further confirmation that the LDA-to-HDA phase transition mostly occurs at the level of the HBN. As we have previously seen, in correspondence with the phase transitions, hyperuniformity is lost and the system is pervaded by long-range density fluctuations. We can now ascribe the loss of hyperuniformity to the sudden enhancement in the percentage of water molecules rearranging their connectivity. We stress here that the key is the celerity that accompanies the increase in C and not the value of C itself. As a matter of fact, upon increasing the pressure we observe that the value of C slowly increases, but HDA has recovered near hyperuniformity.²⁸ Overall, the percentage of water molecules that change their bonded neighbor(s) increases from $\sim 2\%$ right after the phase transition to $\sim 4\%$ at $P = 2$ GPa. Therefore, we can conclude that near hyperuniformity does not require a static network but can be accommodated also when the HBN is dynamic and part of the water molecules keeps changing their connectivity, in agreement with ref 31.

At higher temperatures, we observe that the value of C in LDA fluctuates around $C = 6\%$, much higher than for the case of $T = 80$ K. This striking difference gains even more weight if we observe that it occurs moving from $T = 80$ K to $T = 100$ K and then stays constant at other temperatures. This suggests that the near hyperuniformity achieved upon cooling the liquid

at $T = 80$ K should not be taken for granted at higher temperatures. While the topology of the HBN for LDA at ambient pressure does not change while increasing the temperature from $T = 80$ K to $T = 140$ K, for $T \geq 100$ K the thermal noise might be high enough to prevent the HBN from dissipating long-range density fluctuations.

In correspondence with the transition pressure, we observe a sudden increase in C and such increment becomes larger at higher temperatures. At the highest pressure, $\sim 9\%$ of water molecules change neighbor(s) at $T = 100$ K (panel b), $\sim 11\%$ at $T = 120$ K (panel c), and $\sim 15\%$ at $T = 140$ K (panel c).

Upon decreasing the pressure, the value of C stays roughly constant at all temperatures until when LDA is recovered. Interestingly, we observe a reduction in the percentage of water molecules that change their neighbor(s).

Translational Multiscale Order. So far, we have inspected the properties of amorphous ices at disjointed length scales. We have probed the short-range order via the local tetrahedrality, the intermediate order via the topology of the HBN, and the long-range order via the hyperuniformity index H . Each length scale provides useful information about the molecular processes involved during the compression/decompression cycles. We now turn our attention to the order metric τ (eq 5), which captures the degree of order/disorder at all length scales.

In Figure 16, we report the profile of the order metric τ computed via eq 5 for the compression/decompression cycles.

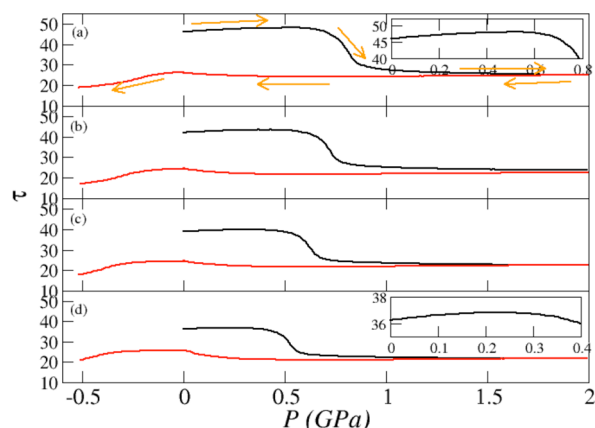


Figure 16. Profile of the translational order metric τ for the compression (black)/decompression (red) cycles at $T = 80$ K in panel a, at $T = 100$ K in panel b, at $T = 120$ K in panel c, and at $T = 140$ K in panel d. The orange arrows define the compression/decompression cycles. The insets report a zoom of the profile of τ at low pressures during the compression.

Panel a refers to $T = 80$ K, panel b to $T = 100$ K, panel c to $T = 120$ K, and panel d to $T = 140$ K, respectively. We can observe that the LDA samples at the four temperatures here inspected markedly differ in terms of metric τ , with higher values in correspondence with lower temperatures. We remark here that, in the thermodynamic limit, the metric τ diverges for perfect crystals while it vanishes identically for spatially uncorrelated systems. Therefore, higher values of τ occurring at lower temperatures indicate the presence of higher degree of order compared to higher temperatures. On the other hand, the LDA samples are mostly indistinguishable at the level of all other order metrics (they are, e.g., very similar in terms of local tetrahedrality as shown in Figure 3 and of large-scale structures

as shown in Figure 13). Upon scanning all length scales, therefore, the metric τ is able to capture the effects of thermal noise that are, otherwise, too feeble to be quantified at disjointed length scales.

Upon increasing the pressure, we observe that τ slightly increases at all temperatures before dropping in correspondence with the phase transition (insets for $T = 80$ K and $T = 140$ K). On the other hand, the short-range order (Figure 3), the network topology (Figure 5), and the H parameter (Figure 13) are mostly insensitive to the applied pressure in these pressure windows. We posit that the increase in τ may be indicative of the tendency of the system exposed to external pressure to rearrange in some crystalline structures, but the local constraints induced by the network of bonds counteract this effect (the loss in configurational entropy would be too high). As expected, the LDA-to-HDA phase transitions are captured by the metric τ at all temperatures with a sudden drop; the resulting HDA samples are characterized by values of τ which are independent of the working temperature, suggesting that the degree of disorder induced by the pressure overcomes the degree of disorder induced by the thermal noise.

The profile of τ differs from the profile of other metrics also upon decompressing the samples. At variance with the short-range order and the H parameter, during the decompression τ shows a negative drift; i.e., it slightly decreases upon decreasing the pressure, before increasing again in the proximity of the recovery of LDA. We hypothesize that the difference in these behaviors is caused by the dilation of the simulation box: locally, water molecules can recover a higher degree of tetrahedrality (Figure 3) because the packing decreases, but at larger scales, the system does not have the time to rearrange in correspondingly more ordered configurations. The increase of local tetrahedrality stabilizes the hydrogen bond network which undergoes fewer variations, as shown by the reduction of the percentage of changed bonds (Figure 15). The network becomes more tetrahedral and slightly less dynamical; the reduction in the changes implies that the network can not acquire configurations able to absorb long-range density fluctuations, and as a result, the system loses hyperuniformity. Upon further decreasing the pressure, the hyperuniform character of the recovered LDA increases as the percentage of changes in the network increase. On the other hand, at the intermediate scale, the system does not have the time to relax and readjust to configurations with lower energies. We posit that this may be related to the fact that the HBN of LDA_{HDA} hosts a slightly larger amount of longer rings than the LDA. That τ metric is able to pick up this residual disorder counterbalancing the increased order at the short and at the long-range.

CONCLUSIONS

We have performed large-scale numerical simulations to investigate the LDA-to-HDA, and the HDA-to-LDA_{HDA} compression/decompression cycles at four temperatures, from $T = 80$ K to $T = 140$ K. Our study pushes the boundary of computational studies in glassy water increasing the number of water molecules commonly adopted in literature by 1 order of magnitude. Such an increase in the number of water molecules is necessary to properly assess the topology of the HBN which is sensitive to finite size effects,³⁰ and the large-scale properties.

The compression/decompression cycles are characterized by evident hysteresis cycles that become wider decreasing the temperatures. This observation is consistent with the recent finding that the TIP4P/2005 model of water has a liquid–liquid critical point.⁴ The hysteresis obtained inspecting the density and the short-range and the long-range order converge to the proximity of the liquid–liquid critical point reported in ref 4. Our approach, therefore, shows that the correlation between structural order and metastable criticality recently explored in the proximity of the liquid–liquid critical point^{17,91} extends into the glassy domain and that signatures of metastability are present in glasses at multiple levels of order.

At all temperatures, at pressures away from the phase transitions, we observe that amorphous ices are nearly hyperuniform and are characterized by a dynamical HBN. Therefore, we can state that nearly hyperuniformity can be hosted in dynamic networks.

In correspondence with the phase transitions, a partial unfreezing of molecular rotations activates a cascade effect that propagates at different length scales: localized molecular rotations induce *sudden* changes in the connectivity that cause a pervasive rewiring of the HBN, ultimately introducing long-range density fluctuations that affect the large-scale properties breaking the hyperuniform character of the samples. In this regard, the fast rate at which changes in connectivity occur (rather than its absolute value) is the key to introducing long-range density fluctuations: in correspondence with the phase transitions, the samples undergo a smaller (larger) amount of changes in connectivity with respect to HDA (LDA_{HDA}), but such changes occur rapidly and the samples are not able to relax, hence undergoing pervasive network rewirings that are otherwise minimal in HDA (LDA_{HDA}).

Finally, we have shown that the translational order metric τ , which captures order at all length scales, is a useful metric to quantify effects that are otherwise too feeble to detect if considered at disjoint scales. Upon decompression, both the short- and the long-range order are captured phase transformations which, on the other hand, are mostly left unseen by the τ metric. This effect should not be attributed to a lack of sensitivity of the τ metric, but rather to the nature of the metric itself: capturing order at the short-, intermediate-, and long-range, the profile acquired by the τ metric indicates that some degree of disorder pervades the samples which counterbalance the increased order at the short- and at the long-range. We intend to further investigate these effects in the future.

Our results provide a detailed understanding of the role (and the effects) of molecular rotations during the glass transition between amorphous ices previously experimentally observed⁸⁵ and can help in rationalizing other transformations triggered by the activation of molecular rotations in materials such as, e.g., hexagonal ice,⁹² clathrates,⁹³ various phases of high-pressure ices,^{94–98} and molecular network-forming materials at large. Nonetheless, our study shows that transformations occurring in amorphous ices occur at multiple, correlated length scales.

AUTHOR INFORMATION

Corresponding Author

Fausto Martelli – IBM Research Europe, WA4 4AD Daresbury, United Kingdom; Department of Chemical Engineering, The University of Manchester, M13 9PL Manchester, United Kingdom; orcid.org/0000-0002-5350-8225; Email: fausto.martelli@ibm.com

Authors

Maud Formanek – IBM Research Europe, WA4 4AD Daresbury, United Kingdom

Salvatore Torquato – Department of Chemistry, Princeton University, Princeton, New Jersey 08544, United States; Department of Physics, Princeton University, Princeton, New Jersey 08544, United States

Roberto Car – Department of Chemistry, Princeton University, Princeton, New Jersey 08544, United States; Department of Physics, Princeton University, Princeton, New Jersey 08544, United States; orcid.org/0000-0001-5243-2647

Complete contact information is available at: <https://pubs.acs.org/10.1021/acs.jpcb.3c00611>

Notes

The authors declare no competing financial interest.

ACKNOWLEDGMENTS

This work was supported by the Hartree National Centre for Digital Innovation, a collaboration between STFC and IBM. S.T. was supported by the U.S. National Science Foundation under Award No. CBET-2133179. R.C. was supported by the Center Chemistry in Solution and at Interfaces funded by the U.S. Department of Energy under Award DE-SC0019394.

REFERENCES

- (1) Salzmann, C. G. Advances in the experimental exploration of water's phase diagram. *J. Chem. Phys.* **2019**, *150*, 060901.
- (2) Palmer, J. C.; Martelli, F.; Liu, Y.; Car, R.; Panagiotopoulos, A. Z.; Debenedetti, P. G. Metastable liquid–liquid transition in a molecular model of water. *Nature* **2014**, *510*, 385–388.
- (3) Sellberg, J. A.; Huang, C.; McQueen, T. A.; Loh, N. D.; Laksmo, H.; Schlesinger, D.; Sierra, R. G.; Nordlund, D.; Hampton, C. Y.; Starodub, D.; et al. Ultrafast x-ray probing of water structure below the homogeneous ice nucleation temperature. *Nature* **2014**, *510*, 381–384.
- (4) Debenedetti, P. G.; Sciortino, F.; Zerze, G. H. Second critical point in two realistic models of water. *Science* **2020**, *369*, 289–292.
- (5) Kringle, L.; Thornley, W. A.; Kay, B. D.; Kimmel, G. A. Reversible structural transformations in supercooled liquid water from 135 to 245 K. *Science* **2020**, *369*, 1490–1492.
- (6) Kim, K. H.; Amann-Winkel, K.; Giovambattista, N.; Spah, A.; Perakis, F.; Pathak, H.; Parada, M. L.; Yang, C.; Mariedahl, D.; Eklund, T.; et al. Experimental observation of the liquid–liquid transition in bulk supercooled water under pressure. *Science* **2020**, *370*, 978.
- (7) Mishima, O.; Calvert, L.; Whalley, E. An apparent first-order transition between two amorphous phases of ice induced by pressure. *Nature* **1985**, *314*, 76.
- (8) Mishima, O.; Calvert, L.; Whalley, E. Melting ice I at 77 K and 10 kbar: A new method of making amorphous solids. *Nature* **1984**, *310*, 393–395.
- (9) Hemley, R. J.; Chen, L. C.; Mao, H. K. New transformations between crystalline and amorphous ice. *Nature* **1989**, *338*, 638–640.
- (10) Mishima, O. Relationship between melting and amorphization of ice. *Nature* **1996**, *384*, 546–549.
- (11) Debenedetti, P. G. Supercooled and glassy water. *J. Phys.: Condens. Matter* **2003**, *15*, R1669–R1726.
- (12) Yue, Y.; Angell, C. A. Clarifying the glass-transition behaviour of water by comparison with hyperquenched inorganic glasses. *Nature* **2004**, *427*, 717.
- (13) Loerting, T.; Giovambattista, N. Amorphous ices: experiments and numerical simulations. *J. Phys.: Condens. Matter* **2006**, *18*, R919.

- (14) Mishima, O.; Stanley, H. E. Decompression-induced melting of ice IV and the liquid-liquid transition in water. *Nature* **1998**, *392*, 164–168.
- (15) Loerting, T.; Fuentes-Landete, V.; Handle, P. H.; Seidl, M.; Amann-Winkel, K.; Gainaru, C.; Böhmer, R. The glass transition in high-density amorphous ice. *J. Non-Cryst. Solids* **2015**, *407*, 423–430.
- (16) Amann-Winkel, K.; Böhmer, R.; Fujara, F.; Gainaru, C.; Geil, B.; Loerting, T. Colloquium: Water's controversial glass transitions. *Rev. Mod. Phys.* **2016**, *88*, 011002.
- (17) Martelli, F.; Leoni, F.; Sciortino, F.; Russo, J. Connection between liquid and non-crystalline solid phases in water. *J. Chem. Phys.* **2020**, *153*, 104503.
- (18) Winkel, K.; Bowron, D. T.; Loerting, T.; Mayer, E.; Finney, J. L. Relaxation effects in low density amorphous ice: two distinct structural states observed by neutron diffraction. *J. Chem. Phys.* **2009**, *130*, 204502.
- (19) Shephard, J. J.; Klotz, S.; Vickers, M.; Salzmann, C. G. A new structural relaxation pathway of low-density amorphous ice. *J. Chem. Phys.* **2016**, *144*, 204502.
- (20) Loerting, T.; Winkel, K.; Seidl, M.; Bauer, M.; Mitterdorfer, C.; Handle, P. H.; Salzmann, C. G.; Mayer, E.; Finney, J. L.; Bowron, D. T. How many amorphous ices are there? *Phys. Chem. Chem. Phys.* **2011**, *13*, 8783–8794.
- (21) Loerting, T.; Salzmann, C.; Kohl, I.; Mayer, E.; Hallbrucker, A. A second distinct structural "state" of high-density amorphous ice at 77 K and 1 bar. *Phys. Chem. Chem. Phys.* **2001**, *3*, 5355–5357.
- (22) Finney, J. L.; Bowron, D. T.; Soper, A. K.; Loerting, T.; Mayer, E.; Hallbrucker, A. Structure of a new dense amorphous ice. *Phys. Rev. Lett.* **2002**, *89*, 205503.
- (23) Mishima, O. Reversible first-order transition between two H₂O amorphs at ~ 0.2 GPa and ~ 135 K. *J. Chem. Phys.* **1994**, *100*, 5910.
- (24) Giovambattista, N.; Sciortino, F.; Starr, F. W.; Poole, P. H. Potential energy landscape of the apparent first-order phase transition between low-density and high-density amorphous ice. *J. Chem. Phys.* **2016**, *145*, 224501.
- (25) Martelli, F.; Giovambattista, N.; Torquato, S.; Car, R. Searching for crystal-ice domains in amorphous ices. *Phys. Rev. Materials* **2018**, *2*, 075601.
- (26) Mollica, E. M.; Russo, J.; Stanley, H. E.; Sciortino, F. Decompression dynamics of high density amorphous ice above and below the liquid-liquid critical point. *Journal of Non-Crystalline Solids: X* **2022**, *13*, 100081.
- (27) Giovambattista, N.; Poole, P. H. Liquid–liquid phase transition in simulations of ultrafast heating and decompression of amorphous ice. *J. Non Cryst. Solids: X* **2021**, *11*, 100067.
- (28) Martelli, F.; Torquato, S.; Giovambattista, N.; Car, R. Large-Scale Structure and Hyperuniformity of Amorphous Ices. *Phys. Rev. Lett.* **2017**, *119*, 136002.
- (29) Gartner, T. E., III; Zhang, L.; Piaggi, P. M.; Car, R.; Panagiotopoulos, A. Z.; Debenedetti, P. G. Signatures of a liquid–liquid transition in an ab initio deep neural network model for water. *Proc. Natl. Acad. Sci. U.S.A.* **2020**, *117*, 26040–26046.
- (30) Martelli, F. Topology and complexity of the hydrogen bond network in classical models of water. *J. Mol. Liq.* **2021**, *329*, 115530.
- (31) Martelli, F. Steady-like topology of the dynamical hydrogen bond network in supercooled water. *PNAS Nexus* **2022**, *1*, pgac090.
- (32) Chiricotto, M.; Martelli, F.; Giunta, G.; Carbone, P. The role of long-range electrostatic interactions and local topology of the hydrogen bond network in the wettability of fully and partially wetted single and multilayer graphene. *J. Phys. Chem. C* **2021**, *125*, 6367–6377.
- (33) Wei, Z.; Chiricotto, M.; Elliott, J. D.; Martelli, F.; Carbone, P. Wettability of graphite under 2D confinement. *Carbon* **2022**, *198*, 132–141.
- (34) Martelli, F.; Calero, C.; Franzese, G. Re-defining the concept of hydration water near soft interfaces. *Biointerphases* **2021**, *16*, 020801.
- (35) Martelli, F.; Crain, J.; Franzese, G. Network Topology in Water Nanoconfined between Phospholipid Membranes. *ACS Nano* **2020**, *14*, 8616–8623.
- (36) Martelli, F. Unravelling the contribution of local structures to the anomalies of water: The synergistic action of several factors. *J. Chem. Phys.* **2019**, *150*, 094506.
- (37) Hejna, M.; Steinhardt, P. J.; Torquato, S. Nearly hyperuniform network models of amorphous silicon. *Phys. Rev. B* **2013**, *87*, 245204.
- (38) Zheng, Y.; Liu, L.; Nan, H.; Shen, Z.-X.; Zhang, G.; Chen, D.; He, L.; Xu, W.; Chen, M.; Jiao, Y.; et al. Disordered hyperuniformity in two-dimensional amorphous silica. *Sci. Adv.* **2020**, *6*, No. eaba0826.
- (39) Zheng, Y.; Chen, D.; Liu, L.; Liu, Y.; Chen, M.; Zhuang, H.; Jiao, Y. Topological transformations in hyperuniform pentagonal two-dimensional materials induced by Stone-Wales defects. *Phys. Rev. B* **2021**, *103*, 245413.
- (40) Chen, D.; Liu, Y.; Zheng, Y.; Zhuang, H.; Chen, M.; Jiao, Y. Disordered hyperuniform quasi-one-dimensional materials. *Phys. Rev. B* **2022**, *106*, 235427.
- (41) Abascal, J. L. F.; Vega, C. A general purpose model for the condensed phases of water: TIP4P/2005. *J. Chem. Phys.* **2005**, *123*, 234505.
- (42) Wong, J.; Jahn, D. A.; Giovambattista, N. Pressure-induced transformations in glassy water: A computer simulation study using the TIP4P/2005 model. *J. Chem. Phys.* **2015**, *143*, 074501.
- (43) Abraham, M. J.; Murtola, T.; Schulz, R.; Páll, S.; Smith, J. C.; Hess, B.; Lindahl, E. GROMACS: High performance molecular simulations through multi-level parallelism from laptops to supercomputers. *SoftwareX* **2015**, *1*, 19–25.
- (44) Nosé, S. A molecular dynamics method for simulations in the canonical ensemble. *Mol. Phys.* **1984**, *52*, 255–268.
- (45) Hoover, W. G. Canonical dynamics: Equilibrium phase-space distributions. *Phys. Rev. A* **1985**, *31*, 1695.
- (46) Berendsen, H. J. C.; Postma, J. P. M.; van Gunsteren, W. F.; DiNola, A.; Haak, J. R. Molecular dynamics with coupling to an external bath. *J. Chem. Phys.* **1984**, *81*, 3684.
- (47) Martelli, F.; Ko, H.-Y.; Oğuz, E. C.; Car, R. Local-order metric for condensed phase environments. *Phys. Rev. B* **2018**, *97*, 064105.
- (48) Martelli, F.; Ko, H.-Y.; Borrallo, C. C.; Franzese, G. Structural properties of water confined by phospholipid membranes. *Front. Phys.* **2018**, *13*, 136801.
- (49) Samatas, S.; Calero, C.; Martelli, F.; Franzese, G. In *Biomembrane Simulations: Computational Studies of Biological Membranes*; Berkovitz, M., Ed.; CRC Press: 2020; pp 69–88.
- (50) Santra, B.; DiStasio, R. A., Jr.; Martelli, F.; Car, R. Local structure analysis in *ab initio* liquid water. *Mol. Phys.* **2015**, *113*, 2829–2841.
- (51) Song, W.-X.; Martelli, F.; Song, Z. Observing the spontaneous formation of a sub-critical nucleus in a phase-change amorphous material from ab initio molecular dynamics. *Mater. Sci. Semicond.* **2021**, *136*, 106102.
- (52) Martelli, F.; Palmer, J. C. Signatures of sluggish dynamics and local structural ordering during ice nucleation. *J. Chem. Phys.* **2022**, *156*, 114502.
- (53) Toffano, A.; Russo, J.; Rescigno, M.; Ranieri, U.; Bove, L. E.; Martelli, F. Temperature-and pressure-dependence of the hydrogen bond network in plastic ice VII. *J. Chem. Phys.* **2022**, *157*, 094502.
- (54) Formanek, M.; Martelli, F. Probing the Network Topology in Network–Forming Materials: the Case of Water. *AIP Adv.* **2020**, *10*, 055205.
- (55) Camisasca, G.; Schlesinger, D.; Zhovtobriukh, I.; Pitsevich, G.; Pettersson, L. G. M. A proposal for the structure of high- and low-density fluctuations in liquid water. *J. Chem. Phys.* **2019**, *151*, 034508.
- (56) Castangna, J.; Martelli, F.; Jordan, K. E.; Crain, J. Simulation of large molecular systems with electronically-derived forces. *Comput. Phys. Commun.* **2021**, *264*, 107959.
- (57) Bakó, I.; Oláh, J.; Lábás, A.; Bálint, S.; Pusztai, L.; Bellissent-Funel, M. C. Water-formamide mixtures: Topology of the hydrogen-bonded network. *J. Mol. Liq.* **2017**, *228*, 25–31.
- (58) Pothoczki, S.; Pusztai, L.; Bakó, I. Variations of the Hydrogen Bonding and Hydrogen-Bonded Network in Ethanol–Water Mixtures on Cooling. *J. Phys. Chem. B* **2018**, *122*, 6790–6800.

- (59) Pothoczki, S.; Pusztai, L.; Bakó, I. Molecular Dynamics Simulation Studies of the Temperature-Dependent Structure and Dynamics of Isopropanol–Water Liquid Mixtures at Low Alcohol Content. *J. Phys. Chem. B* **2019**, *123*, 7599–7610.
- (60) Li, L.; Zhong, J.; Yan, Y.; Zhang, J.; Xu, J.; Francisco, J. S.; Zeng, X. C. Unraveling nucleation pathway in methaneclathrate formation. *Proc. Natl. Acad. Sci. U.S.A.* **2020**, *117*, 24701–24708.
- (61) Le Roux, S.; Jund, P. Ring statistics analysis of topological networks: New approach and application to amorphous GeS₂ and SiO₂ systems. *Comput. Mater. Sci.* **2010**, *49*, 70–83.
- (62) Yuan, X.; Cormack, A. N. Efficient algorithm for primitive ring statistics in topological networks. *Comput. Mater. Sci.* **2002**, *24*, 343–360.
- (63) Chihai, V.; Adams, S.; Kuhs, W. F. Molecular dynamics simulations of properties of a (001) methane clathrate hydrate surface. *Chem. Phys.* **2005**, *317*, 208–225.
- (64) Hegedüs, J.; Elliott, S. R. Microscopic origin of the fast crystallization ability of Ge–Sb–Te phase-change memory materials. *Nat. Mater.* **2008**, *7*, 399–405.
- (65) Blaineau, S.; Jund, P. Vibrational signature of broken chemical order in a GeS₂ glass: A molecular dynamics simulation. *Phys. Rev. B* **2004**, *69*, 064201.
- (66) Wooten, F.; Winer, K.; Weaire, D. Computer Generation of Structural Models of Amorphous Si and Ge. *Phys. Rev. Lett.* **1985**, *54*, 1392.
- (67) Wooten, F.; Weaire, D. Modeling Tetrahedrally Bonded Random Networks by Computer. *Solid State Phys.* **1987**, *40*, 1.
- (68) Djordjevic, B. R.; Thorpe, M. F.; Wooten, F. Computer model of tetrahedral amorphous diamond. *Phys. Rev. B* **1995**, *52*, 5685.
- (69) Barkema, G. T.; Mousseau, N. Event-Based Relaxation of Continuous Disordered Systems. *Phys. Rev. Lett.* **1996**, *77*, 4358.
- (70) Barkema, G. T.; Mousseau, N. High-quality continuous random networks. *Phys. Rev. B* **2000**, *62*, 4985–4990.
- (71) Hudson, T. S.; Harrowell, P. A systematic enumeration of local topological relaxation mechanisms in amorphous networks and their efficiency in network relaxation. *J. Chem. Phys.* **2007**, *126*, 184502.
- (72) Opletal, G.; Petersen, T. C.; Snook, I. K.; McCulloch, D. G. Modeling of structure and porosity in amorphous silicon systems using Monte Carlo methods. *J. Chem. Phys.* **2007**, *126*, 214705.
- (73) King, S. V. Ring Configurations in a Random Network Model of Vitreous Silica. *Nature* **1967**, *213*, 1112–1113.
- (74) Rahman, A.; Stillinger, F. H. Hydrogen-Bond Patterns in Liquid Water. *J. Am. Chem. Soc.* **1973**, *95*, 7943–7948.
- (75) Guttman, L. Ring structure of the crystalline and amorphous forms of silicon dioxide. *J. Non-Cryst. Solids* **1990**, *116*, 145–147.
- (76) Franzblau, D. S. Computation of ring statistics for network models of solids. *Phys. Rev. B* **1991**, *44*, 4925.
- (77) Wooten, F. Structure, odd lines and topological entropy of disorder of amorphous silicon. *Acta Cryst. A* **2002**, *58*, 346–351.
- (78) Luzar, A.; Chandler, D. Hydrogen-bond kinetics in liquid water. *Nature* **1996**, *379*, 55–57.
- (79) Prada-Gracia, D.; Shevchuk, R.; Rao, F. The quest for self-consistency in hydrogen bond definitions. *J. Chem. Phys.* **2013**, *139*, 084501.
- (80) Shi, R.; Russo, J.; Tanaka, H. Common microscopic structural origin for water's thermodynamic and dynamic anomalies. *J. Chem. Phys.* **2018**, *149*, 224502.
- (81) Torquato, S.; Stillinger, F. H. Local density fluctuations, hyperuniformity, and order metrics. *Phys. Rev. E* **2003**, *68*, 041113.
- (82) Atkinson, S.; Zhang, G.; Hopkins, A. B.; Torquato, S. Critical slowing down and hyperuniformity on approach to jamming. *Phys. Rev. E* **2016**, *94*, 012902.
- (83) Torquato, S.; Zhang, G.; Stillinger, F. H. Ensemble theory for stealthy hyperuniform disordered ground states. *Phys. Rev. X* **2015**, *5*, 021020.
- (84) Foffi, R.; Sciortino, F. Structure of high-pressure supercooled and glassy water. *Phys. Rev. Lett.* **2021**, *127*, 175502.
- (85) Shephard, J.; Salzmann, C. G. Molecular reorientation dynamics govern the glass transitions of the amorphous ices. *J. Phys. Chem. Lett.* **2016**, *7*, 2281–2285.
- (86) Lin, C.; Yong, X.; Tse, J. S.; Smith, J. S.; Sinogeikin, S. V.; Kenney-Benson, C.; Shen, G. Kinetically Controlled Two-Step Amorphization and Amorphous-Amorphous Transition in Ice. *Phys. Rev. Lett.* **2017**, *119*, 135701.
- (87) Torquato, S. Hyperuniform states of matter. *Phys. Rep.* **2018**, *745*, 1–95.
- (88) Jiao, Y.; Lau, T.; Hatzikirou, H.; Meyer-Hermann, M.; Corbo, J. C.; Torquato, S. Avian photoreceptor patterns represent a disordered hyperuniform solution to a multiscale packing problem. *Phys. Rev. E* **2014**, *89*, 022721.
- (89) Klatt, M. A.; Lovrić, J.; Chen, D.; Kapfer, S. C.; Schaller, F. M.; Schönhöfer, P. W. A.; Gardiner, B. S.; Smith, A.; Schröder-Turk, G. E.; Torquato, S. Universal hidden order in amorphous cellular geometries. *Nat. Commun.* **2019**, *10*, 1–9.
- (90) Zhang, G.; Martelli, F.; Torquato, S. The structure factor of primes. *J. Phys. A: Math. Theor.* **2018**, *51*, 115001.
- (91) Foffi, R.; Sciortino, F. Correlated Fluctuations of Structural Indicators Close to the Liquid–Liquid Transition in Supercooled Water. *J. Phys. Chem. B* **2023**, *127*, 378–386.
- (92) Haida, O.; Matsuo, T.; Suga, H.; Seki, S. Calorimetric study of the glassy state X. Enthalpy relaxation at the glass-transition temperature of hexagonal ice. *J. Chem. Thermodyn.* **1974**, *6*, 815–825.
- (93) Suga, H.; Matsuo, T.; Yamamuro, O. Thermodynamic study of ice and clathrate hydrates. *Pure Appl. Chem.* **1992**, *64*, 17–26.
- (94) Salzmann, C. G.; Kohl, I.; Loerting, T.; Mayer, E.; Hallbrucker, A. The low-temperature dynamics of recovered ice XII as studied by differential scanning calorimetry: a comparison with ice V. *Phys. Chem. Chem. Phys.* **2003**, *5*, 3507–3517.
- (95) Salzmann, C. G.; Mayer, E.; Hallbrucker, A. Thermal properties of metastable ices IV and XII: Comparison, isotope effects and relative stabilities. *Phys. Chem. Chem. Phys.* **2004**, *6*, 1269–1276.
- (96) Salzmann, C. G.; Radaelli, P. G.; Finney, J. L.; Mayer, E. A calorimetric study on the low temperature dynamics of doped ice V and its reversible phase transition to hydrogen ordered ice XIII. *Phys. Chem. Chem. Phys.* **2008**, *10*, 6313–6324.
- (97) Shephard, J. J.; Salzmann, C. G. The complex kinetics of the ice VI to ice XV hydrogen ordering phase transition. *Chem. Phys. Lett.* **2015**, *637*, 63–66.
- (98) Zimoń, M. J.; Martelli, F. Molecular rotations trigger a glass-to-plastic fcc heterogeneous crystallization in high-pressure water. *J. Chem. Phys.* **2023**, *158*, 114501.